Spatial Heterogeneity Alters the Dynamics of the Yeast Galactose Switch: Insights from 4D RDME–ODE Hybrid Simulations

Tianyu Wu[1,2], Marie-Christin Spindler[3,2], Emmy Earnest[4], Henry Li[2], Zane R. Thornburg[5,6], Julia Mahamid[3,7,2], Zaida Luthey-Schulten[8,2,1*]

1 Center for Biophysics and Quantitative Biology, University of Illinois at Urbana–Champaign, Urbana, IL, USA
2 National Science Foundation Science and Technology Center for Quantitative Cell Biology, Beckman Institute for Advanced Science and Technology, University of Illinois at Urbana–Champaign, Urbana, IL, USA
3 Molecular Systems Biology Unit, European Molecular Biology Laboratory (EMBL), Heidelberg, Germany
4 Department of Physics, University of Illinois at Urbana–Champaign, Urbana, IL, USA
5 Beckman Institute for Advanced Science and Technology, University of Illinois at Urbana-Champaign, Urbana, IL, USA
6 Cancer Center at Illinois, University of Illinois at Urbana-Champaign, Urbana, IL, USA
7 Cell Biology and Biophysics Unit, European Molecular Biology Laboratory (EMBL), Heidelberg, Germany
8 Department of Chemistry, University of Illinois at Urbana–Champaign, Urbana, IL, USA

* zan@illinois.edu

Abstract

We present the first 4D simulations of the galactose switch in *Saccharomyces cerevisiae* using a hybrid framework that integrates reaction diffusion master equations (RDMEs) and ordinary differential equations (ODEs). Using the GPU-based Lattice Microbes program, genetic information processes were simulated stochastically while a simplified metabolism was modeled deterministically. Cell geometry was constructed based on recently acquired cryo-electron tomograms(cryo-ET), which allows us to quantify and differentiate between cytosolic ribosomes and endoplasmic reticulum(ER) associated ribosomes. This allows us to simulate realistic numbers of available ribosomes for ER-associated translation of proteins destined for the cell membrane, like the galactose transporter G2. Our simulations show that an extracellular 11 mM galactose triggers expression of 10k-15k galactose transporters within 60 minutes. We also benchmarked the multi-GPU solver's performance under various spatial decompositions. Our work underscores the challenges of whole cell modeling of eukaryotic cells and the effects of their inherent spatial heterogeneity.

Author summary

Cells must quickly adapt when their food source changes. In baker's yeast, a genetic switch turns on dozens of genes so the cell can use the sugar galactose instead of glucose. We built the first four-dimensional computer model that follows every key molecule in a realistic, tomogram-based yeast cell as this switch is involved. The model combines random, molecule-by-molecule chemistry for rare events with faster, deterministic equations for abundant reactions, and runs on graphics-processing units powerful enough to simulate an entire cell in an hour. By explicitly distinguishing ribosomes that float freely from those anchored on the endoplasmic reticulum, we tracked where the galactose transporter Gal2 is made and how it travels to the cell membrane. The simulations predict that about 10,000–15,000 transporters appear within an hour after the cell senses 11 mM galactose, and reveal that the maze-like endoplasmic reticulum slows their delivery. Our framework shows how cellular geography alters genetic information processing production and paves the way for whole-cell simulations of more complex organisms.

Introduction 1

Cellular reaction–diffusion processes unfold in a crowded, architecturally complex milieu, yet most stochastic simulations still assume a well-stirred cytoplasm in which every molecule experiences identical reaction propensities [1–3]. This simplification is especially untenable for eukaryotes, where membranes partition the cytosol into organelle-defined micro-domains that impose diffusion barriers and segregate molecular species. Spatial heterogeneity can therefore reshape noise propagation, alter local reaction kinetics, and even drive qualitative shifts in network behavior that a well-mixed chemical master equation (CME) cannot capture. The RDME method provides a lattice-based framework capable of resolving these effects with higher fidelity.

The budding-yeast (*Saccharomyces cerevisiae*) galactose switch offers an ideal benchmark for exploring spatial effects on gene regulation. Its circuitry has been dissected genetically, biochemically, and quantitatively for more than four decades [4, 5]. A well-parameterized well-stirred CME–ODE hybrid model already exists [1], providing a stringent baseline against which spatial extensions can be judged. Moreover, recent cryo-ET tomograms supply high-resolution geometries of wild-type yeast cells, including portions of the nuclear envelope, mitochondria, and ER [6]. These data allow the galactose switch to be embedded in a three-dimensional lattice that respects realistic compartment boundaries and volumetric fractions.

Here we construct a spatially resolved RDME–ODE hybrid model of the galactose switch. The well-stirred scheme is transplanted onto the cryo-ET-reconstructed yeast lattice, and an ER network is built and added for membrane protein translation and transport. Reactions are partitioned into (i) deterministic ODEs for fast or high-copy processes—e.g. galactose transport and metabolism—and (ii) stochastic RDME reactions for low-copy, noise-sensitive events such as transcription, translation, and regulator–promoter interactions. Each cellular compartment—plasma membrane, cytosol, nucleus, mitochondria, vacuole, and ER—is assigned appropriate diffusion coefficients and reactions, enabling diffusion-driven exchange across adjacent voxels. By explicitly modeling ER architecture and ribosome allocation, the new framework ameliorates a key limitation of previous well stirred scheme [1].

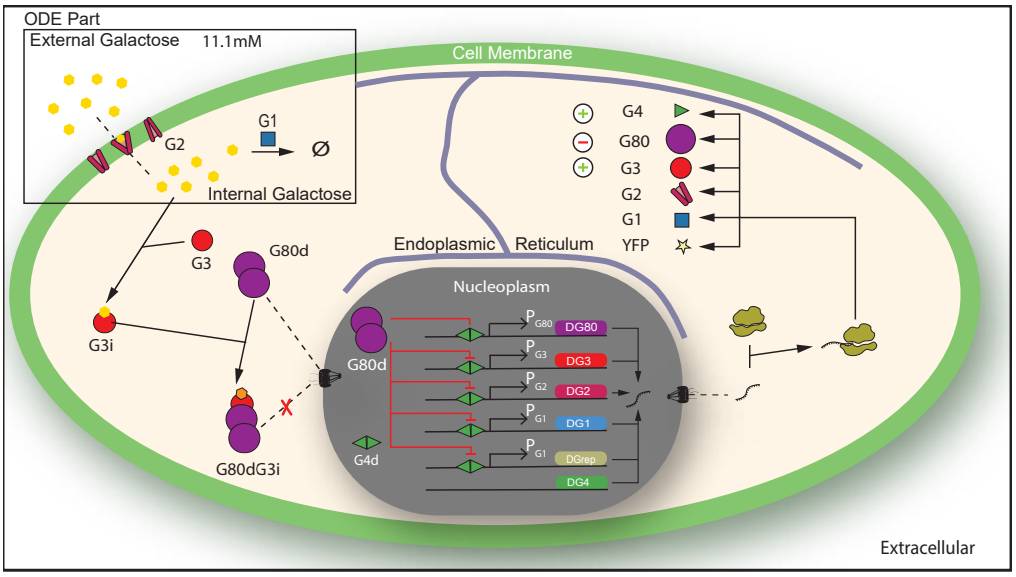

Figure 1. Schematic of the budding-yeast galactose switch. ODE-treated metabolic reactions are boxed at top left. Positive regulators G4d and G3 activate transcription, whereas G80d represses it. The suffix "d" indicates the dimeric state.

The galactose switch governs expression of genes needed for galactose utilization once glucose, the preferred carbon source, is depleted. The network comprises 39 molecular species and 75 reactions arranged in two positive and one negative feedback loops that respond dynamically to extracellular galactose [4, 5]. As illustrated in Fig. 1, four core genes—*GAL1* (DG1), *GAL2* (DG2), *GAL3* (DG3), and *GAL80* (DG80)—plus the transcriptional activator *GAL4* (DG4) and an optional reporter (DGrep) are induced with the same promoter region as DG1. Dimeric activator G4d binds promoters (except its own) to initiate transcription. In the presence of galactose, inducer G3 binds the sugar and sequesters repressor G80d from diffusing into the nucleus, sustaining expression. G1 catalyses the first metabolic step, whereas G2, translated at the ER, traffics to the plasma membrane to import galactose.

We validated regulatory dynamics by comparing the RDME–ODE results with those of the previously published well-stirred CME–ODE model [1]. Incorporating ER geometry revealed that membrane trafficking of the galactose transporter Gal2 is significantly delayed, while reduced ER-bound ribosome density modulates translational throughput. Explicitly modeling the fraction of active ribosomes further demonstrated how ribosome availability tunes system responsiveness [7, 8]. Leveraging an optimized multi-GPU solver on NVIDIA A100 and H100 hardware, we achieved substantial speed-ups, making routine simulation of full 4D yeast cells feasible.

Collectively, our spatially resolved model shows that organelle-level architecture is not a dispensable detail but a determinant of stochastic regulatory outcomes. Spatial heterogeneity (i) shifts mRNA and protein abundances—especially for the galactose transporter, (ii) delays its delivery to the plasma membrane, and (iii) modulates the system's sensitivity to extracellular galactose. These findings underscore the necessity of incorporating realistic geometry in computational studies of gene regulation in yeast and beyond.

Materials and methods

57

0.1 Reconstruction of Yeast Cell Geometry Using Cryo-ET

The 3D geometry of budding yeast cells was reconstructed using cryo-ET data acquired from vitrified yeast samples prepared via cryo-focused ion beam (cryo-FIB) milling. Detailed information used in present work was previously reported in Earnest et al. [6]. Briefly, a tomographic volume of approximately $2.04 \times 1.91 \times 0.242\ \mu m^3$ at a pixel size of 5.31 Å, was reconstructed using the IMOD tomography package [9]. Due to the limited field of view, missing structures outside the tomographic volume were extrapolated based on known volumetric and structural constraints (described below). The reconstructed geometry was downsampled to a lattice resolution of 28.67 nm to balance simulation accuracy and computational efficiency.

0.1.1 Extrapolation of Missing Geometries for Ellipsoid Structures

As the field of view in the original tomogram was limited, the extrapolation of missing or incomplete geometries was performed by fitting ellipsoidal models to the segmented tomographic data. The partial nuclear envelope and plasma membrane were initially represented as binary masks derived from segmentation as in Fig 2(a). To construct an ellipsoidal structure, nine parameters were required: three for radii, three for rotational angles, and three for the center coordinates of the ellipsoid. To represent the cytoplasm, cytoplasmic membrane, nucleoplasm, and nuclear envelope, we used partial geometric data from the tomogram and applied the `scipy.optimize.minimize` function to fit ellipsoidal masks onto the existing structures. The ellipsoidal fitting process followed the methodology described in Earnest et al. [6]. We further implemented 139 nuclear pores extrapolated based on the nuclear pore density (nuclear pores are represented as white cross on the nuclear envelope as in Fig 2(c))

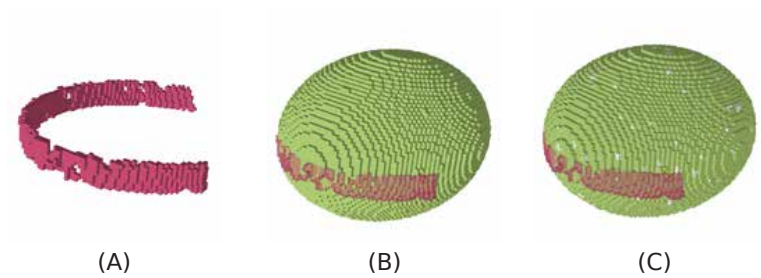

Figure 2. Geometric Reconstruction of the Nuclear Envelope.(A) Segmented slice from cryo-electron tomography (cryo-ET) data.(B) Ellipsoidal fitting of the nuclear envelope.(C) Addition of nuclear pore complexes as white crosses to the reconstructed envelope.

0.1.2 Construction of Mitochondrial, Vacuole, and Cell Wall Geometries

As the present cryo-ET data only contains a fraction of the mitochondrial network, vacuole, and the cell wall. We utilized the volumetric percentage of each organelle to extrapolate the missing geometries [10].

- **Cell Wall**: The cell wall was assumed to share the same rotational angles and center as the plasma membrane, and its radii were back-calculated based on the volumetric occupancy (15.9%).
- **Vacuole**: The vacuole occupies 7.8% of the total cell volume. Since budding yeast typically contains a single vacuole, its geometry was constrained to an ellipsoidal

shape with semi-major axes (a, b) randomly selected between 0.9 and 1.0, and the third radius $c = 1/(ab)$ to maintain the volume. Rotational angles are randomly determined to avoid vacuole overlap with nucleus.

- **Mitochondria**: Mitochondria occupy 1.6% of the total volume. Based on BioNumbers data ID:103068 [11, 12], there are approximately three mitochondria per yeast cell. The total mitochondrial volume was divided equally among these three compartments, with each ellipsoidal mitochondrion randomly placed within the cytoplasmic region using random orientations while ensuring no overlap with existing intracellular structures.

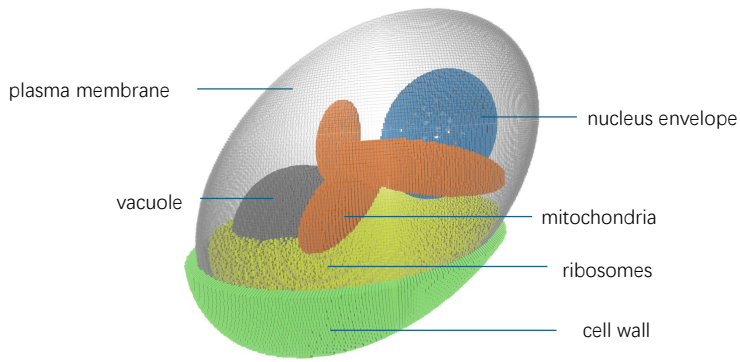

Figure 3. 3D Spatial Geometry of Budding Yeast. To enhance visibility, only a subset of ribosomes is displayed. The vacuole is shown in gray, the nuclear envelope in blue with nuclear pores as empty holes. Mitochondria appear in orange, ribosomes in yellow, the plasma membrane in transparent gray, and the cell wall in green/lime.

0.1.3 Modeling Ribosome Distribution without ER

The ribosome dimensions in budding yeast are approximately $25.4\,\text{nm} \times 27.8\,\text{nm} \times 26.7\,\text{nm}$ [13]. Given that our lattice spacing is $28\,\text{nm} \times 28\,\text{nm} \times 28\,\text{nm}$, each ribosome was modeled as occupying one lattice cube. In the model without ER, we use 180,000 cytoplasmic ribosomes as reported in BioNumbers [11, 14]. Ribosomes were uniformly distributed throughout the cytoplasm by randomly selecting lattice sites not overlapping with existing intracellular structures. Although alternative reports indicate ribosome counts ranging from 105,000 to 380,414 [15–17], simulations showed that variations within this range had minimal impact on the final results, as the number of translating ribosomes during the first 60 minutes remained below 150 (see Figure S1).

0.1.4 Modeling Geometries of Endoplasmic reticulum

To model the geometry of ER, we developed a novel method based on available electron and fluorescence miscroscopy data [18]. Studies on budding yeast have shown that the ER differs significantly from the tubular network structures typically observed in mammalian and plant cells [19, 20]. The yeast ER consists primarily of large curved sheets near the plasma membrane (peripheral ER, pmaER) and around the nuclear envelope (cisternal ER, cecER), connected by sparse tubular structures (tubular ER,

tubER) [18, 21]. The volumetric occupancy of the entire ER was estimated at 2.2% [10]. Additionally, the ER was decomposed into three regions: pmaER: 50% of total ER volume; tubER: 30% of total ER volume; cecER: 20% of total ER volume. Also, the average thickness of pmaER and cecER sheets were 35.6 nm and 36.0 nm, respectively, with a 33.0 nm gap between the ER sheets and the adjacent membranes [22].

To construct the pmaER, we generated an ellipsoidal shell with the thickness of one lattice cube, reducing each radius by two lattice cubes compared to the plasma membrane:

$$\begin{aligned}\text{pmaShell} = \text{Ellipsoid}\Big[&\big(a_{\text{plasmamem}} - 1,\ b_{\text{plasmamem}} - 1,\ c_{\text{plasmamem}} - 1\big),\\ &\text{(plasma membrane angles)},\\ &\text{(plasma membrane center)}\Big]\\ -\ \text{Ellipsoid}\Big[&\big(a_{\text{plasmamem}} - 2,\ b_{\text{plasmamem}} - 2,\ c_{\text{plasmamem}} - 2\big),\\ &\text{(plasma membrane angles)},\\ &\text{(plasma membrane center)}\Big].\end{aligned} \tag{1}$$

The pmaER was then constructed by randomly assigning a number n of fragments with individual volumes $\{V_i : i \in [1, n]\}$ in the pmaShell such that $\sum_{i=1}^{n} V_i = V_{\text{pmaER}}$. The breadth-first search algorithm was applied to iteratively grow regions within the pmaShell until the desired volume V_i was reached. This process was repeated n times, ensuring no overlap between fragments:

$$\begin{aligned}\text{pmaFragments}_i \cap \text{pmaFragments}_j = \emptyset \quad (i \neq j),\\ \text{pmaER} = \sum_{i=1}^{n} \text{pmaFragments}_i.\end{aligned} \tag{2}$$

The same procedure was applied to construct the cecER, using adjusted parameters. The tubER was modeled as tubular structures with cross-sectional diameters d randomly selected from the range 60–100 nm [23]. The total tubER length was calculated as $L = \frac{V_{\text{tub}}}{d^2}$. Tubules were generated by connecting randomly selected pairs of pmaER and cecER fragments until the available length was exhausted. The final structure is shown in Figure 4(A).

0.1.5 Modeling ER-associated Ribosomes

To approximate the number of ER-associated ribosomes, we used previously published cryo-ET data of *S. cerevisiae* [24] and analyzed the proximity of the peptide exit tunnel sites of all ribosomes to the nearest ER membrane (Figure 5). The dense globular ribosomes are clearly discernible in the tomograms (Figure 5A), enabling their localization with DeePiCt [25], which employs a 3D Convolutional Neuronal Network (CNN). The CNN prediction output was manually curated to achieve roughly a 95 % completeness of ribosome annotations in the data (Figure 5B). Based on all detected ribosomes, we generated a subtomogram average of 10,723 ribosomes with a resolution of 11.1 Å [24]. We determined the position of the peptide exit tunnel for each ribosome based on this average (Figure 5 (C)). Next, MemBrain seg [26] was used to automatically annotate all membranes in the tomograms and the 'find connected regions' ImageJ plugin (`https://github.com/fiji/VIB/blob/master/src/main/java/util/Find_Connected_Regions.java`) was used to assign labels to the different

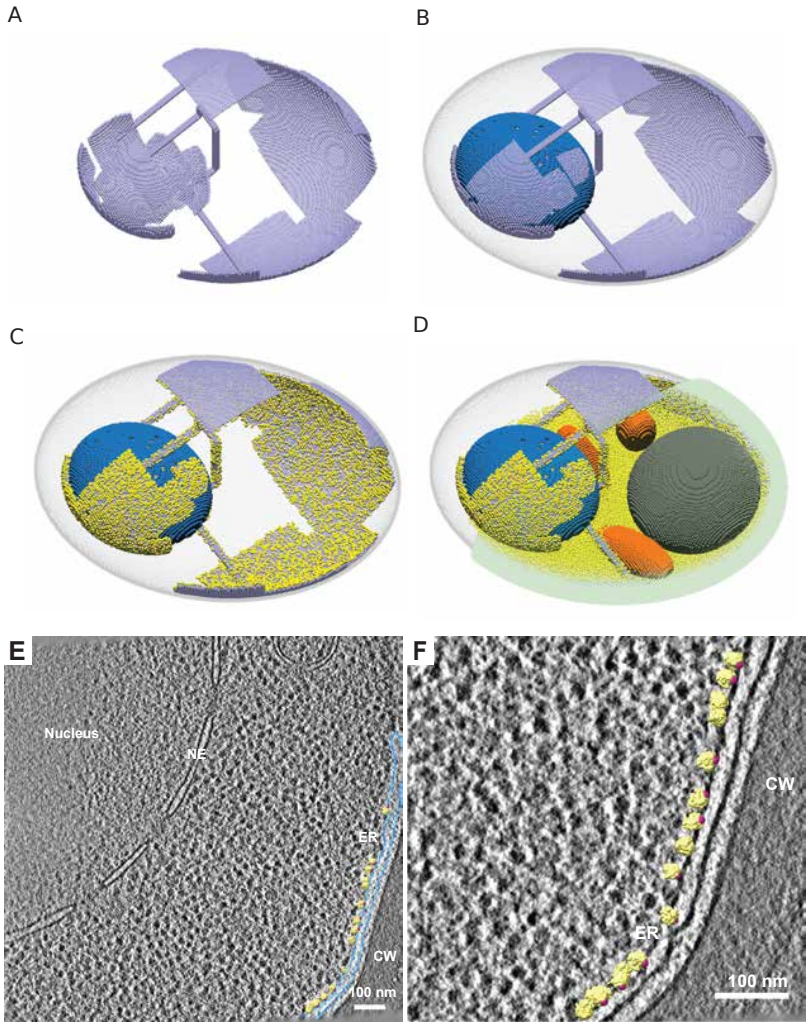

Figure 4. 3D modeling of the ER and ER-attached ribosome density experimental results. (A) Reconstructed ER with pmaER, tubER, and cecER. (B) ER wtih nucleus envelope and plasma membrane. (C) ER-attached ribosomes; the pmaER, which faces the plasma membrane, has very few ribosomes, so none are attached in the geometric model. (D) Final spatial geometry model for simulation with ER; for clarity, only a portion of the cyto-ribosomes are shown.(E) Ribosomes with an exit tunnel (magenta sphere) less than 8 nm from the closest ER membrane back-projected into the tomogram in accordance with their original position. The binary ER membrane segmentation is overlaid in blue. (F) Zoom in of (E) showing the orientation of the peptide exit tunnels with respect to the ER membrane.

organelle membranes and export the binary mask of only the ER membranes which were present in 6 out of the 9 reconstructed tomograms. Napari [27] (`https://zenodo.org/records/15029515`) was used to manually clean up any errors in the ER segmentations. Finally, the distances of all peptide exit tunnels to the closest ER membrane were calculated using a custom python script. Based on the histogram of these distances, a cut-off distance of 8 nm was determined to identify translating ribosomes on the surface of the ER (Figure 4E-F).

The surface area of the ER was calculated using the RegionFeaturesJ plugin (`https://github.com/ijtools/RegionFeaturesJ/releases/tag/v0.3.1`) in ImageJ to report the number of translating ribosomes per ER surface area. The regions analyzed in our cryo-ET data predominantly represent cortical ER (referred to as pmaER in [22]) and ER continuous with the nuclear envelope (cecER). Potential tubular ER (tubER) is not continuous with the nuclear envelope and can be hard to discern from Golgi. It was excluded from our calculations for stringency reasons.

A previous study using plastic-sections electron microscopy reports higher numbers for ribosomes located on the ER membrane surface [22] compared to the cryo-ET derived values determined in the present study (ER-associated ribosome density in Table 1). This discrepancy likely arises from different criteria for defining an ER-ribosome association. In the present study, a ribosome translating into the ER is defined by a distance of the peptide exit tunnel of below 8 nm, taking the orientation of the individual ribosomes into account. In contrast, the previous study includes all ribosomes within 5 nm of the ER membrane regardless of their orientation, thus potentially including ribosomes that were not actively translating into the ER.

ER Region	**Literature Range**	**ER high-ribo value**	**ER low-ribo value**
cecER	600–1100	850	424
pmaER	550–900	725	362
tubER	250–400	325	162

Table 1. Comparison of Ribosome Surface Densities on ER Regions.

To account for these discrepancies in ER-associated ribosome counts, we ran our present model under two regimes. For the first regime, which included the ER (termed "ER sim high-ribo"), we used the previously reported [22] average ribosome density value (see Table 1). We then re-ran the simulation with the number of translating ribosomes on the ER surface determined based on our cryo-ET data (termed "ER sim low-ribo"; see Table 1). Here, we treated the determined value as the density of pmaER-associated ribosomes and adapted this value for the cecER and tubER proportionally. In both simulations, ribosomes were randomly assigned to lattice sites according to the calculated surface areas of the respective ER regions taking into account that the ER membrane proximal to the cell membrane is not decorated with ribosomes. The final number of ER-bound ribosomes was 15,452 for the "ER sim high-ribo" runs and 7,715 for the "ER sim low-ribo" runs, which are within range of the median abundance (17,267) of sec61 protein(YLR378C)- the only essential component of the Sec61 ER translocation complex- as reported in the Saccharomyces Genome Database [28]. Sec61 is the only essential component of Sec61 ER translocation complex. In both ER-inclusive regimes, translation of the galactose transporter G2 was restricted to ER-bound ribosomes, leading to co-translational insertion into the ER and subsequent trafficking through the secretory pathway to the plasma membrane.

0.1.6 Description of the Final Yeast Cell Geometry

The final reconstructed yeast cell geometry shown in Figure 4d, consisting of 10 spatial regions (extracellular region, cell wall, plasma membrane, cytoplasm, nuclear envelope,

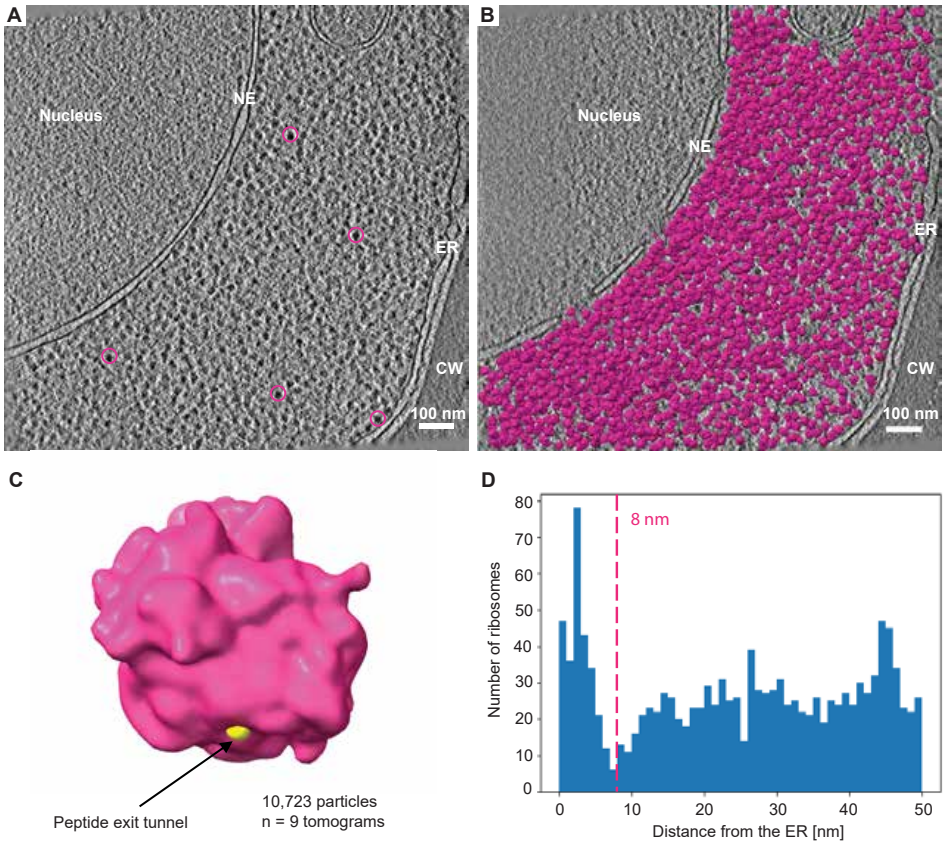

Figure 5. Number of Translating Ribosomes on ER Membranes Based on cryo-ET of *S. cerevisiae*. (A,B) Tomographic slice of an *S. cerevisiae* cell depicting the cytosol crowded with ribosomes (dense globular particles), the ER, the cell wall (CW) and the nucleus with the nuclear envelope (NE). (A) Individual ribosomes are encircled in magenta. (B) Example of comprehensive 3D annotation of all 80S ribosomes (magenta). (C) Ribosome subtomogram average from wildtype *S. cerevisiae* cells. Particle number, determined resolution and number of tomograms are indicated. The average was used to determine the coordinate of the peptide exit tunnel (centroid of the yellow sphere). (D) Histogram of the distances of all peptide exit tunnels to a binary segmentation of the closest ER membrane. A cut-off distance of 8 nm was determined to identify translating ribosomes on the surface of the ER.

nucleoplasm, mitochondria, vacuole, cytosolic ribosomes and ER-associated ribosomes), was integrated into the Lattice Microbes(LM) v2.5 to perform spatially resolved stochastic simulations. For simulations including the ER, the reconstructed geometry included 16 spatial regions (extracellular region, cell wall, plasma membrane, cytoplasm, nuclear envelope, nucleoplasm, mitochondria, vacuole, ribosomes, cecER, cecER_ribosomes, tubER, tubER_ribosomes, pmaER and pmaER_ribosomes).

0.2 Simulating Spatially Resolved Stochastic Chemical Kinetics Using the Reaction-Diffusion Master Equation (RDME)

The RDME provides a powerful framework for performing spatially-resolved stochastic simulations of intracellular processes, combining particle-level stochastic reactions with spatial diffusion dynamics. In this study, we applied the RDME approach to simulate transcription, translation, and regulator-promoter interactions in the galactose switch. These simulations were performed using the LM software [1,29,30], which supports both well-stirred and spatially-resolved models. For RDME/spatially resolved models, LM explicitly incorporates spatial effects by discretizing the cellular volume into subvolumes v centered on a cubic lattice grid. Reactions occurring within each subvolume are assumed to be well-stirred and are simulated stochastically using the Gillespie algorithm [31], while particle diffusion between adjacent subvolumes is modeled using a diffusion operator (see Equation 3).

$$\begin{aligned}\frac{dP(\mathbf{x},t)}{dt} &= \mathbf{R}P(\mathbf{x},t) + \mathbf{D}P(\mathbf{x},t)\\ &= \sum_{v}^{V}\sum_{r}^{R}\Big[-a_r(\mathbf{x}_v)P(\mathbf{x}_v,t) + a_r(\mathbf{x}_v-\mathbf{S}_r)P(\mathbf{x}_v-\mathbf{S}_r,t)\Big]\\ &\quad+\sum_{v}^{V}\sum_{\xi}^{i,j,k}\sum_{\alpha}^{N}\Big[-d^{\alpha}x_v^{\alpha}P(\mathbf{x},t) + d^{\alpha}\big(x_{v+\xi}^{\alpha}+1\big)P\big(\mathbf{x}+1_{v+\xi}^{\alpha}-1_v^{\alpha},t\big)\Big]. \quad (3)\end{aligned}$$

The RDME governing stochastic dynamics can be expressed as a sum of two terms: (1) the CME in each subvolume which describes the reaction happens in it and(2) a diffusion term accounting for inter-subvolume molecular movement. Specifically, the local CME governs stochastic chemical reactions within each subvolume v, while the diffusion operator describes the movement of particles of type along the x, y, and z directions, represented by indices i, j, k. The state of the system x, encapsulates the molecular counts of all species (genes, RNAs, and proteins) at any given time. Spatial heterogeneity arises naturally in these simulations, capturing differences in molecular distributions across subcellular regions, such as nuclear and cytoplasmic zones.

0.3 Using the Multi-GPU Solver for RDME Simulation

To scale spatial stochastic simulations of the galactose switch in yeast, we implemented the `MGPUMpdRdmeSolver`, a multi-GPU extension of the existing `MpdRdmeSolver` in LM by Hallock *et al.* [30] to allow hybrid simulations. Our implementation partitions the three-dimensional simulation domain along the Z-axis, distributing workloads across multiple GPUs while minimizing inter-device communication overhead(see Figure 6).

Each GPU independently processes its assigned subdomain, exchanging only the necessary boundary data during synchronization phases. To optimize runtime performance, we leverage asynchronous CUDA streams that overlap computation with communication in the overlapping regions. Peer-to-peer (P2P) memory transfers via NVLink or PCIe further accelerate data exchange between GPUs by avoiding costly

host memory transfers. Moreover, custom packing and unpacking routines compress boundary updates into contiguous buffers, thereby reducing data movement. Figure 6 illustrates how a four-GPU framework partition the simulation space and exchanges boundary area data.

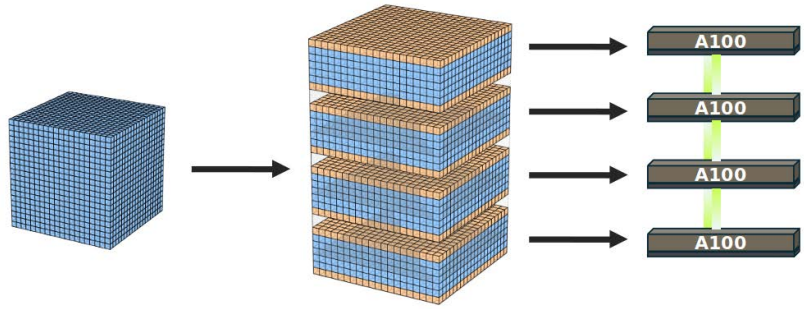

Figure 6. Latticed Cellular Space Partition in Multi-GPU Solvers. The continuous cellular space is first coarse-grained into a 3D lattice(in blue, left). This lattice is then evenly partitioned into four slices, each including two additional apron regions on the top and bottom of the cell region (shown in orange) to allow inter-slice communication. Each slice is assigned to a separate A100 GPU for parallel computation. After local computations are completed, neighboring slices exchange information about particles in the apron regions to ensure consistency across GPU boundaries.

Each GPU is bounded to a dedicated CPU thread, and these threads are synchronized by `pthread` barriers and `mutexes` that prevent race conditions. Within each thread, CUDA synchronization APIs are used to maximize parallelism.

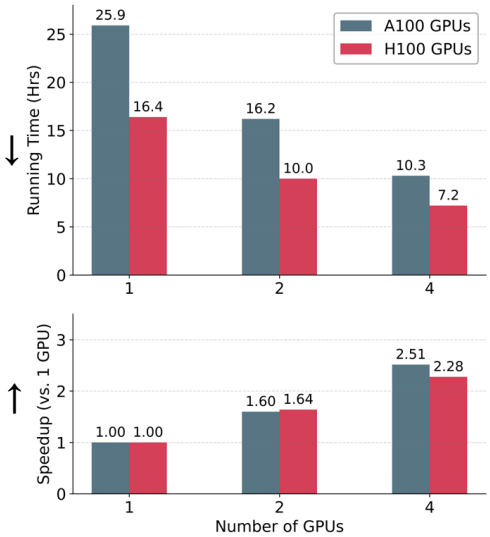

Figure 7. Computational Performance of Yeast RDME-ODE Simulations on A100 vs. H100 GPUs. Simulations represent 1 hour of biological time and were conducted using 1, 2, and 4 GPUs. The top panel shows the total wall-clock runtime in hours, with H100 GPUs consistently outperforming A100 GPUs across all configurations. The bottom panel illustrates the speedup relative to the 1-GPU runtime for each hardware type. Both GPU architectures exhibit sublinear scaling, with A100 achieving a maximum speedup of 2.51× and H100 reaching 2.28× with 4 GPUs.

We run the RDME simulations on Delta (AMD EPYC 7763 “Milan” CPU and

Ampere 100 GPU) and Delta AI (NVIDIA Grace CPU and Hopper 100 GPU). Figure 7 shows the benchmark statistics of running single-GPU and multi-GPU solvers on our yeast model. The four-GPU solver demonstrates a 2.5-fold speedup compared to the 1-GPU solver. Consequently, multi-GPU solvers can enable simulations of larger cellular volumes and longer timescales, fully capturing the spatial heterogeneity of the yeast galactose network while maintaining high computational efficiency.

0.4 Modeling Stochastic Processes in the Yeast Galactose Switch Using an RDME Framework

In our present model, genetic information processing reactions (i.e., transcription, translation, regulator-promoter interactions, mRNA degradation, protein complex formation, and protein complex degradation) were represented as stochastic processes using a RDME framework (see Tables S5-S10). RDME simulations of the genetic information processing reactions were resolved with subvolume precision, meaning that reactions were only allowed to take place within a specific cubic location (see Supplementary Tables S5-S10, Region variable). Additionally, diffusion behaviors were specified for each molecular species including both diffusion within a given region type and diffusion across boundaries between different regions. (See Table S12).

The regulator-promoter interaction events were defined to occur within the nucleoplasm region for regulatory genes DG1, DG2, DG3, DG80 and DGrep (fluorescence reporter gene), and the non-regulatory gene DG4 (see Table S5). For regulatory genes, each had 3 states: free (labeled as "DGX"), activated (labeled as "DGX:G4d") and repressed (labeled as "DGX:G4d:G80d"). When genes were in activated states, the transcription started and ended with the release of the messenger RNAs (mRNAs) in the same sublattice volume. For the non-regulatory gene DG4 (Gal4), we modeled the transcription to take place stochastically with a given rate (see Table S6). The messengers then diffuse from nucleoplasm to cytoplasm through nuclear pores. In the cytoplasm, mRNAs are either degraded (see Table S7) or diffuse into and bind to ribosomes for translation (see Table S8). Protein complexes modeled included 3 proteins: G3, G4 and G80 (see Table S9). For instance, G3 can bind to the cytoplasmic galactose (GAI) to form a complex G3i, which can further bind to the G80d in the cytoplasm. The G3iG80d complex prevents G80d from transporting through the nuclear pore into the nucleoplasm, thereby inhibiting the repressive effects of G80d.

0.5 Modeling Deterministic Processes in the Yeast Galactose Switch Using an ODE Framework

The transportation of extracellular galactose into the yeast cell via G2 and galactose metabolism into galactose-1-phosphate via G1 were modeled deterministically (see Table S11). As our present model does not explicitly account for downstream metabolic pathways, the metabolic product galactose-1-phosphate is currently represented as a dead-end.

0.6 Defining Initial Conditions for Abundances of Chemical Species

For the initial abundance of each species, we used the values reported in Ramsey *et al.* [4], rounding each to the nearest integer(see Table S2-S3). For molecular species that are present in multiple cellular compartments, we distributed their initial counts proportionally according to regional volumes. The initial counts used in the RDME simulations are summarized in Table S2-3 in SI. Gene copy numbers were set to one and

placed randomly in the nucleoplasm in their repressed state (GalX:G4d:G80d), consistent with biological expectations in the absence of induction. These repressed genes are assumed to be immobile (non-diffusive) throughout the simulation. In contrast, G4, which is not under regulatory control in the model, is constitutively transcribed. For the mutant conditions, we removed regulatory constraints on G3 and G80, allowing them to be transcribed continuously. All mRNAs were initialized with zero copy numbers, except for mRNA for G3 and Grep (R3, Rrep). The protein species G1, G3, and the reporters (GFP/YFP) were randomly distributed in the cytoplasm at initialization, while G2 was localized to the plasma membrane. G4d was initialized in the nucleoplasm. G80 and G80d were randomly distributed between cytoplasm and nucleoplasm in proportion to the volume ratio of the two regions. Ribosomes were also placed in their respective compartments to support mRNA translation. The internal galactose concentration was initialized to zero, reflecting experimental conditions in which cells were first cultured in a non-inducing medium (raffinose) before galactose exposure. External galactose was treated as a constant input set by the user throughout the simulation. The choice to start from a repressed gene state and zero internal galactose reflects the experimental protocol [4], where the induction dynamics were measured upon switching cells from raffinose to galactose.

0.7 Combining Stochastic and Deterministic Reactions into a Hybrid RDME-ODE Method

We employed the hybrid RDME-ODE framework to efficiently simulate spatially resolved gene expression and metabolism in budding yeast, using stochastic methods for low-copy processes and ODEs for high-copy metabolic reactions. Notably, the bimolecular reaction $G3 + GAI \rightarrow G3i$, characterized by a low copy number of G3 and a high copy number of GAI, poses computational challenges when directly included in the RDME framework. Direct incorporation significantly slows down the RDME simulations and leads to spatially crowded subvoxels due to excessive galactose molecules. To address this, we converted the bimolecular reaction into a pseudo-first-order reaction $G3 \rightarrow G3i$ by redefining its kinetic parameter as $k' = k \cdot [\text{GAI}]$, where k represents the original kinetic rate constant and [GAI] denotes the intracellular concentration of GAI. This modification maintains biological accuracy while significantly enhancing computational efficiency. This conversion and parameter update are handled dynamically by the *setReactionRate* function within the simulation hook, newly implemented here for compatibility with multi-GPU solvers.

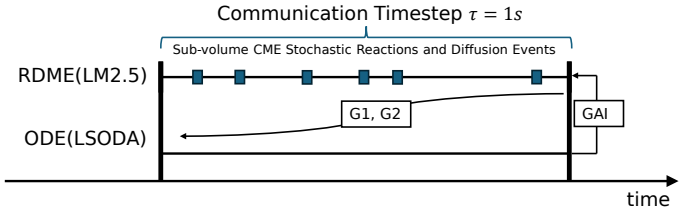

Figure 8. Hook schematics for the communication between RDME and ODE simulation.

Communication between the RDME and ODE solvers occurs at regular intervals $\tau = 1s$ as depicted in Figure 8, determined based on the separation of timescales between slow stochastic reactions and faster deterministic metabolic processes [1]. At each communication step, the state of the RDME system (e.g., local particle counts) is

updated to reflect the results of the ODE solver, and then the ODE part is performed, and communicate the species counts back to RDME and updates the kinetic parameters in RDME simulation.

Algorithm 1 Hybrid RDME-ODE Simulation of the Galactose Switch Using Lattice Microbes

```
Initialize simulation environment
Load spatial model and define domains (extracellular, cell wall, nucleus, etc.)
Specify molecular species
Define biochemical reactions (transcription, translation, degradation, etc.)
Assign diffusion coefficients
procedure HybridSimulation
    Initialize ODE system for transport and metabolism
    Initialize RDME system for spatial stochastic reactions
    while t < t_max do
        Execute RDME step (reaction-diffusion process)
        if time interval== hook interval then
            Update ODE state using RDME molecular counts
            Integrate ODE system over the interval
            Update RDME reaction rates based on ODE outputs
        end if
        Store system statistics and trajectory data
    end while
end procedure
```

0.8 Simulation Design and Analysis of Spatially-Resolved Galactose Switch Dynamics

We ran the present RDME-ODE models of the galactose switch in yeast for a total of 60 minutes of biological time. Due to the stochastic nature of our model's framework, we ran 5 number of simulation replicates, recording population averages and standard deviations for each outcome. Simulations were conducted under physiologically relevant conditions (i.e., an extracellular galactose concentration of 11.1mM [0.2% w/v]) [4].

Our first set of analyses examined how spatial heterogeneity alters galactose-switch dynamics. We ran RDME-ODE simulations in a voxelized yeast geometry and, for direct comparison, a CME-ODE model that used the same kinetic parameters but assumed a well-mixed cytoplasm [1]. For CME-ODE, we executed 20 60-min replicates at 11.1 mM extracellular galactose, recording time-series for GAL2 activation state, GAL2 mRNA and protein levels, and intracellular galactose concentrations. Due to computational expensive for RDME-ODE scenario, we ran 5 replicates per case. Differences between frameworks were quantified from replicate means and standard deviations to isolate the specific contribution of spatial resolution.

Our second set of analyses focused on the effects of explicitly modeling the ER in the yeast cellular geometry. To determine the influence of the ER on membrane protein transport, we compared RDME-ODE simulations under two distinct scenarios: with and without ER. In the ER-inclusive model, we further explored two distinct sub-scenarios that differ in the number and distribution of ER-associated ribosomes available for membrane translation. In all three cases, kinetic and diffusion parameters were kept constant, with biologically realistic spatial constraints applied only in the ER-inclusive conditions.

Our final set of analyses was focused on how limiting the number of ribosomes

available to translate galactose-related mRNA affected the protein production. The galactose switch system operates under translational constraints because its mRNAs must compete with those of other cellular genes for access to the shared pool of free ribosomes. Technically, not all free ribosomes can be used to translate mRNA for the galactose switch system, as other cellular processes occupy the translational machinery. In these analyses we assume that the ribosomes that translate the mRNA for the galactose switch system should roughly be proportional to the mRNA abundance for the galactose switch system compared to all the mRNA in the yeast [7, 8]. We estimated the effective ribosome number using mRNA abundance to determine the number of available ribosomes for the galactose switch system. We therefore assume that 2,102 ribosomes (0.0117% of total ribosomes) are utilized while the rest are set into a silent state that only serve as an obstacle for diffusion in the cytoplasm. Finally, as the GALrep has the same promoter as GAL1, we used the mRNA abundance of GAL1 for GALrep.

Results

366

0.9 Intracellular spatial heterogeneity enhances galactose transport in RDME-ODE compared to CME-ODE models

Introducing spatial heterogeneity reshapes the dynamics of galactose switch system, with marked divergence from the well-mixed CME-ODE model emerging after around 15 min of simulation. As a representative of the system-wide changes, we focus on results related to galactose transporter G2. First, although the gene began in the inhibited state (i.e., DG2:G4d:G80d), when compared to the CME-ODE framework [1], transporter gene exhibited a significantly higher probability (78.3% time with $p < 0.05$) of transitioning to and being kept in the activated state in the RDME-ODE model(Figure 9A). Consequently, we observed the mRNA counts of G2 were constantly reached higher level(87.7 % time with $p < 0.05$) (Figure 9B). Consequently, the number of transporter G2 in the plasma membrane significantly increased (78.3% time with $p < 0.05$) when compared to the well-stirred model (Figure 9C). As would be expected, the increase in membrane-bound G2 molecules was accompanied by a significant increase (82.7 % time with $p < 0.05$) in intracellular galactose concentration (Figure 9D).

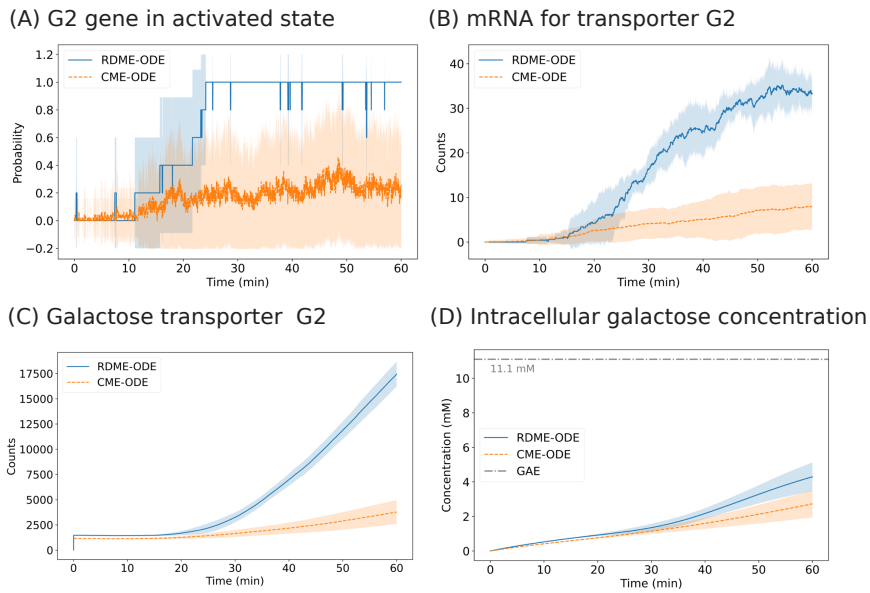

Figure 9. Comparison of G2-related species and intracellular galactose (GAI) concentration between our RDME-ODE model and the CME-ODE model [1]. (A) Probability of the transporter gene in the activated state (DG2:G4d). (B) Abundance of total mRNA (R2). (C) Abundance of galactose transporter G2. (D) Total intracellular galactose concentration(sum of GAI, G1GAI, G2GAI, and G3i). Both simulations were performed for 60 minutes with 11.1 mM constant external galactose concentration. For the RDME-ODE simulations, we ran five replicates using the geometry without the ER. Identical kinetic parameters were applied to both models, except that the first-order diffusion reaction governing G80 transport between the cytoplasm and nucleus in the CME-ODE model was replaced with explicit diffusion events.

0.10 Explicitly Modeling Endoplasmic Reticulum Induces Temporal Delays in Membrane Protein Transport

We began by partitioning the ER into three morphologically distinct domains—the nuclear-envelope-associated ER (nucER), the plasma-membrane-associated ER

(pmaER), and the tubular ER (tubER)—and then populated each domain with ribosomes at densities taken either from West *et al.* [22] or from our own cryo-ET measurements.

To assess how the ER constrains membrane-protein abundance, we ran RDME-ODE simulations in three settings: a no-ER control and two ER-inclusive scenarios that differed only in the abundance of ER-bound ribosomes ("ER high-ribo" and "ER low-ribo"; see Methods). All kinetic and diffusive parameters were identical across runs; only the ER-inclusive models incorporated spatially explicit ER geometries and the restriction that galactose transporter G2 translation occurs exclusively on ER-attached ribosomes.

Although the total number of G2 that reached the plasma membrane within the first 20 minutes did not differ significantly among the three conditions, the ER-inclusive simulations exhibited a marked reduction in membrane-localized transporters after 30 minutes ($p<0.05$; Figure 10D). This shortfall arises from two factors: (a) the smaller pool of ER-associated ribosomes, which lengthens the time free GAL2 mRNA spends searching and binding to the free ribosomes(see Figure 10F), and (b) the longer, tortuous diffusion path imposed by ER-mediated trafficking. Consistent with the diminished transporter abundance, intracellular galactose levels fell sharply in ER models, averaging $\tilde{2}$ mM in ER high-ribo and $\tilde{1}$ mM in ER low-ribo versus $\tilde{4}.5$ mM in the no-ER control ($p<0.05$ after 40 min; Figure 10E).

Varying the density of ER-attached ribosomes further clarified the impact of translation capacity on system behavior. Free and ribosome-bound G2 mRNA counts were statistically indistinguishable between ER high-ribo and ER low-ribo simulations (mean $p > 0.5$, $p > 0.1$; Figures 10A–B). Nonetheless, ER high-ribo produced $\tilde{2}$,000 additional transport proteins in the cytoplasm/ER (Figure 10C) and correspondingly more transporters at the membrane (Figure 10D), resulting in a relatively higher final intracellular galactose concentration (Figure 10E). Taken together, these results demonstrate that both the presence of ER geometries and the local density of ER-associated ribosomes critically modulate G2 trafficking efficiency and, consequently, the rate of galactose import.

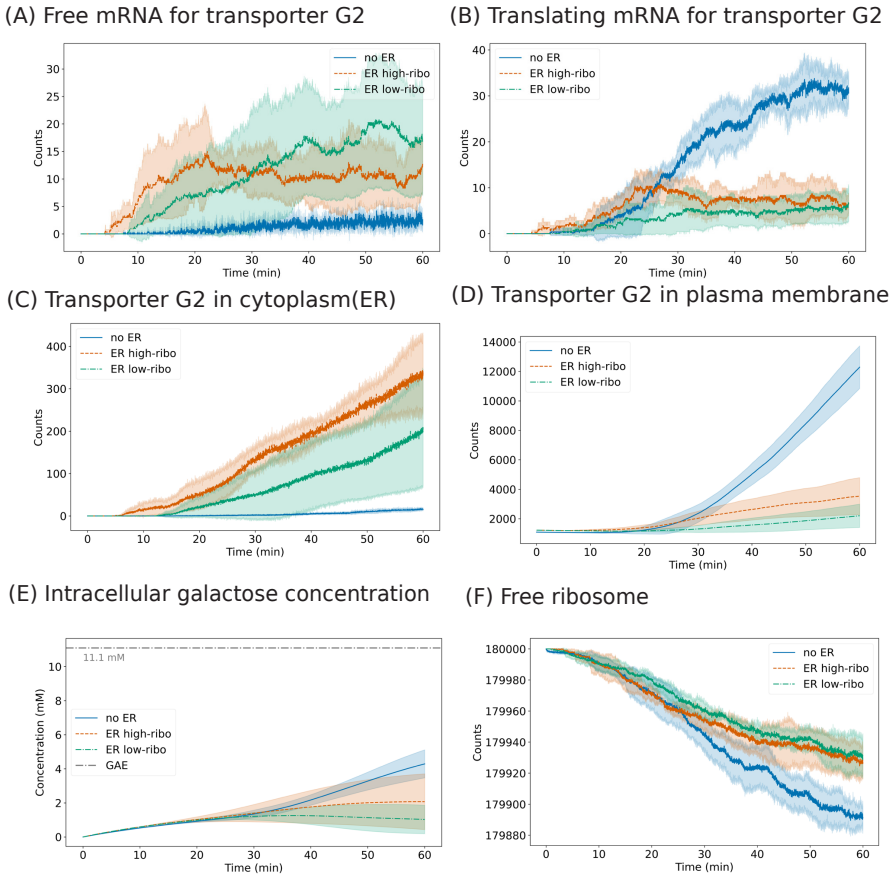

Figure 10. Comparison of intracellular galactose (GAI) and transporter(G2) related species between the model without ER and ER with different ER-associated ribosome density for ER high-ribo and ER low-ribo. (A) the abundance of free mRNA for transporter(R2). (B) the abundance of translating mRNA for transporter(R2). (C) the abundance of transporter in cytoplasm (including ER if present). (D)the abundance of galactose transporter G2 in plasma membrane. (E) Intracellular galactose concentration. (F) the abundance of free ribosomes not binding to any mRNA.

0.11 Limiting the Number of Available Ribosomes Significantly Constrains Protein Production

Next, we restricted the number of translation-ready ribosomes for the purpose of simulating biologically-relevant conditions with genes in the galactose switch competing ribosomes with other genes in the yeast and compared these simulations with the previous simulations including all ribosomes. We observed significantly higher (85.5% time with $p < 0.05$) free G2 mRNA counts (Figure 11A) and lower (62.3% time with $p < 0.05$) actively translating G2 mRNA counts (Figure 11B) in the restricted ribosome scenario. Unsurprisingly, the total number of galactose transporters in the restricted ribosome scenario was significantly lower (71.6 % time with $p < 0.05$; Figure 11C). This difference total G2 transporters led to the restricted ribosome scenario having lower intracellular galactose concentrations (Figure 11D).

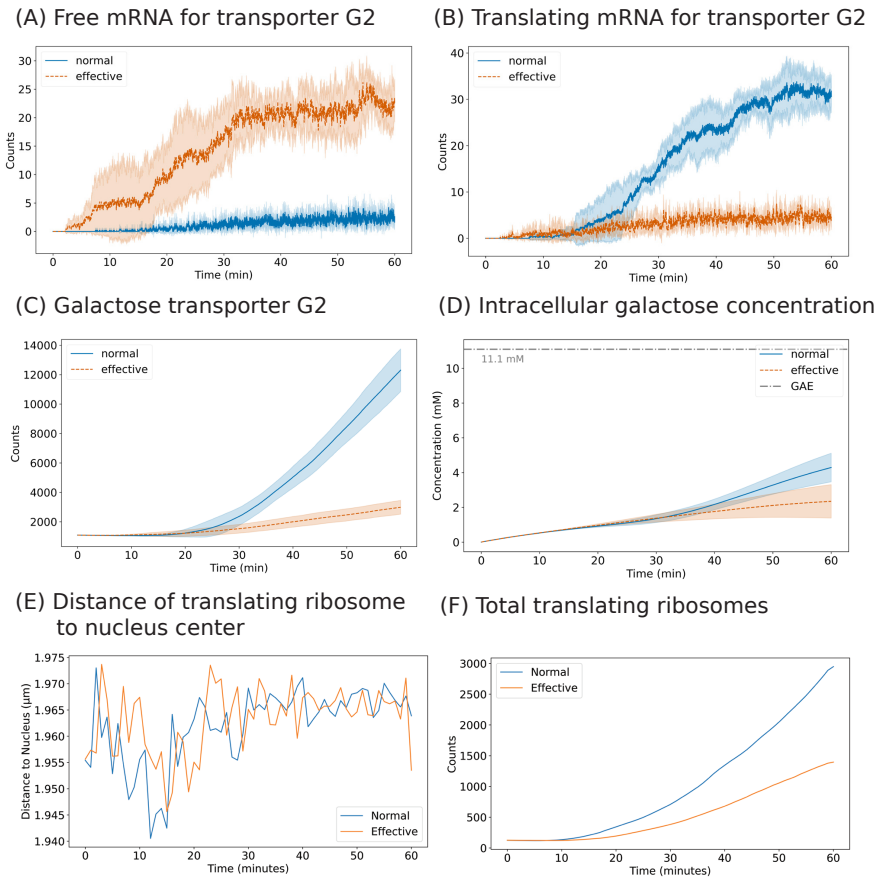

Figure 11. Effects of Limiting Ribosome Availability on Galactose-Related Species. (A) the abundance of free mRNA for transporter G2. (B) the abundance of translating mRNA for transporter G2 (C) the abundance of galactose transporter G2. (D) the concentration of intracellular galactose GAI. (E) the average distance of translating ribosomes to the center of nucleus. (F)the average accumulated counts of translating ribosomes.

Discussion

428

Our study presents a significant advancement in the computational modeling of yeast galactose switch by integrating spatial heterogeneity in cell geometry, the presence of ER and ER-associated ribosomes and the competing for free ribosomes with mRNA out of galactose switch.

The integration of spatial heterogeneity revealed several critical insights that would have otherwise been overlooked in well-mixed schemes (CME-ODE). First, our spatially resolved simulations demonstrated that the physical separation of molecular species across subcellular compartments alters reaction dynamics compared to well-mixed CME-ODE models. We demonstrated these differences by highlighting the discrepancies in galactose transporter related species, with the conclusion that intracellular concentrations of galactose were significantly increased in our spatially heterogeneous scenarios.

For comparison between RDME-ODE and CME-ODE, the reason why DG2 has a higher probability of remaining in activated state is primarily due to an initial asymmetry in diffusion fluxes across nuclear envelope. Specifically, the repressor G80d has a greater likelihood of diffusing out of the nucleoplasm rather than into it, resulting in an increased probability of gene activation(Figure 9A).

This asymmetry can be quantified using average search times. For G80d diffusion within the nucleoplasm (Figure S2A), we consider the time required to locate a nuclear pore from the nucleus center. Given that the nuclear dimensions along the a, b, and c axes are roughly equal, we approximate the nucleus as a sphere with radius $R_{\text{nuc}} = 1\ \mu m$. For particles diffusing inside a spherical domain of radius R with absorbing patches (pores) of fractional area ϕ, the average escape time (τ) can be estimated using the well-established formula [32, 33]:

$$\tau = \frac{R^2}{3D\phi} \tag{4}$$

For our model, the fractional area occupied by nuclear pores is:

$$\phi = \frac{A_{\text{pores}}}{S_{\text{nuc}}} = \frac{N \cdot \pi \cdot r_{\text{pore}}^2}{4\pi R_{\text{nuc}}^2} = \frac{139 \times \pi \times 0.042^2 \mu m^2}{4\pi \times 1^2 \mu m^2} \approx 0.06 \tag{5}$$

Thus, the average time for G80d to diffuse out of the nucleus is:

$$\tau_{\text{out}} = \frac{(1\mu m)^2}{3 \times 1\mu m^2/s \times 0.06} \approx 5.44s \tag{6}$$

When treated as a first-order reaction, as we have in the CME-ODE model, this yields a rate constant:$k_{\text{out}} \approx \tau_{\text{out}}^{-1} \approx 11.03/min$

Conversely, for G80d diffusing into the nucleus through nuclear pore complexes, the particle must first locate a pore and subsequently enter it. By approximating nuclear pores as absorbing spheres and applying the Smoluchowski 3D first-passage diffusion approximation, the average inward diffusion time (τ_{in}) is:

$$\tau_{\text{in}} \approx \frac{V_{\text{cyto}}}{4\pi D R_{\text{nuc}} \phi} \tag{7}$$

Assuming a spherical yeast cell with radius $R_{plasma\,mem} = 2\,\mu$m, the estimated average time for G80d to diffuse into the nucleus is approximately 38.1s, corresponding to the following: $k_{\text{in}} = \tau_{\text{in}}^{-1} \approx 1.57/min$

This substantial asymmetry in reaction kinetics contrasts sharply with the symmetric diffusion conditions in the CME-ODE model, where $k^{\text{CME-ODE}}\text{in} = k^{\text{CME-ODE}}\text{out} = 500/min$. This kinetic asymmetry explains the initial

drastic reduction in G80d abundance observed in the RDME-ODE model relative to the CME-ODE model.

Genes maintain higher probabilities of remaining in activated states primarily due to reduced propensities, making state transitions less likely. Specifically, the effective propensities for first-order and second-order reactions are diminished in spatially heterogeneous environments due to reactant compartmentalization and the reduced volume from the entire cell to individual subvoxels.

Explicitly, for first-order reactions, the propensities are:

$$a_{\text{CME}} = k \cdot N_{a,\text{total}} \tag{8}$$

$$a_{\text{RDME}} = k \cdot N^{i}_{a,\text{subvoxel}} \tag{9}$$

where k is the reaction rate constant, Na, total is the total reactant count in the whole cell, and $N^{i}_{a,\text{subvoxel}}$ is the reactant count in subvoxel i. Thus, the relationship is:

$$a\text{RDME} = a_{\text{CME}} \cdot \frac{1}{N_{\text{subvoxels}}} < a_{\text{CME}}, \quad N_{\text{subvoxels}} > 1 \tag{10}$$

For second-order reactions, propensities are similarly adjusted:

$$a_{\text{CME}} = k \cdot \frac{N_{a,\text{total}} \cdot N_{b,\text{total}}}{V_{\text{total}}} \tag{11}$$

$$a_{\text{RDME}} = k \cdot \frac{N_{a,\text{subvoxel}i} \cdot Nb, \text{subvoxel}j}{V\text{subvoxel}_i} \tag{12}$$

Here, $N_{b,\text{total}}$ and $N_{b,\text{subvoxel}j}$ represent the total and subvoxel-specific counts of the second reactant, respectively; $V\text{total}$ and $V_{\text{subvoxel}i}$ denote the total cell and subvoxel volumes. Assuming well-mixed conditions, $Ni, \text{total} = N_{i,\text{subvoxel}i} \cdot N\text{subvoxels}$ and $V_{\text{total}} = V_{\text{subvoxel}i} \cdot N\text{subvoxels}$, yielding:

$$a_{\text{RDME}} = a_{\text{CME}} \cdot \frac{1}{N_{\text{subvoxels}}} < a_{\text{CME}} \tag{13}$$

The increased probability of gene activation leads to enhanced mRNA production in the RDME-ODE model. Subsequently, the high local concentration of mRNA in the cytoplasmic compartments facilitates efficient translation, resulting in accelerated G2 protein synthesis compared to the CME-ODE model (Figure 9C). In the spatial model, G2 proteins experience the directional diffusion toward the cell membrane in $\tau = \frac{\langle l^2 \rangle}{6D} \approx 1.5\,\text{s}$, establishing concentration gradients that further enhance transport efficiency. These spatial effects eventually lead to elevated intracellular galactose concentrations in FIgure 9D, highlighting how spatial organization can influence the dynamics of the galactose switch system. Additionally, we used the RDME-ODE model to reproduce the rapid increase in reporter levels (GFP/YFP) observed in the mutant strain compared to the wild type shown in Figure S3, consistent with the original experimental findings [4].

Second, our incorporation of the ER revealed a temporal delay in membrane protein transport that is absent in models lacking spatial resolution or ER geometries. The requirement for G2 mRNA to locate ER-bound ribosomes, followed by the translated protein's extended diffusion path through the ER network to reach the plasma membrane, led to the reduced transporter abundance on plasma membrane (Figure 10D). Therefore, intracellular galactose concentrations were lower compared with no ER cases(Figure 10E). This reduction occurs for two reasons. First, since there are far fewer ER-associated ribosomes available for translation, free mRNA has a harder time finding a ribosome to initiate translation, compared to the no-ER case shown in

Figure 10A and Figure 10B. Second, ER-mediated diffusion through complex, irregular, and tubular geometries inherently requires more time than direct cytoplasmic diffusion. At the current diffusion rate, a transporter takes roughly 1 second to reach the plasma membrane. Additionally, transporters tended to accumulate in plasma membrane regions proximal to tubular ER structures(see Supporting videos S3).

Third, our analysis of ribosome availability demonstrated that protein production is significantly constrained by the limited pool of ribosomes available for translating specific mRNAs. Additionally, this difference led to differences in intracellular galactose concentrations. By incorporating a more realistic estimate of effective ribosome numbers based on mRNA abundance data, we observed substantially reduced protein production of G2(Figure 11A).

While our model marks a significant advance in spatially resolved biochemical simulations by integrating reaction-diffusion and deterministic dynamics in a realistic cellular architecture, several limitations remain that present opportunities for future refinement. First, the computational intensity of RDME-ODE simulations restricted our ability to perform extensive replicates or to perform simulations for extended periods of time. Second, the spatial architecture used here was derived from a single static tomographic snapshot, which does not capture the dynamic structural remodeling that occurs during membrane trafficking, organelle biogenesis, or nuclear reorganization. These additional processes are likely to influence molecular diffusion and reaction rates. Third, while our model captures essential aspects of gene expression and molecular interactions, it currently omits several biologically important layers of regulation. These include post-translational modifications, complexes binding like degradosome or splicesome and compartment-specific metabolic fluxes, which are critical for understanding the full spectrum of cellular function.

In conclusion, our hybrid RDME-ODE approach to modeling the yeast galactose switch highlights the importance of incorporating spatially heterogeneity in the simulation of cellular dynamics. The methodologies developed here provide a foundation for future whole-cell modeling efforts that integrate structural, molecular, and systems-level data to achieve a comprehensive understanding of cellular function for budding yeast.

Supporting information

S1 File. Simulation paramters and supplementary simulation. This file contains information on species names, reactions, and simulation parameters such as kinetic rates and diffusion coefficients. It also includes additional simulation results referenced in the main text.

S2 Video Videos for the RDME-ODE simulation trajectory in 60 minutes for normal geometry.

S3 Video Videos for the RDME-ODE simulation trajectory in 60 minutes for ER-included geometry.

S4 Video Videos for the RDME-ODE simulation trajectory in 60 minutes for normal geometry with effective ribosomes.

S5 Repository. Source code Github repository with instructions to run the code: https://github.com/Luthey-Schulten-Lab/Yeast_Galactose_Switch_RDMEODE.git

Acknowledgments

The authors thank Abner Apsley for his valuable suggestions on manuscript revisions and overall guidance. We also thank David Bianchi and Troy Brier for their support and tutorship in using Lattice Microbes. Computational resources were provided by the National Center for Supercomputing Applications (NCSA) at the University of Illinois at Urbana–Champaign, including access to the Delta and Delta AI systems, supported by NSF ACCESS and the NSF Innovative HPC program. We are grateful to Sara Kathrin Goetz for acquiring the cryo-electron tomograms, the EMBL cryo-EM platform for instrument access, and Thomas Hoffmann and the EMBL IT team for computational support. J.M. was supported by a European Research Council Starting Grant (3DCellPhase 760067) and EMBL. This project was supported by the National Science Foundation Science and Technology Center for Quantitative Cell Biology (DBI-2243257). T.W., M.C.S., and Z.L.S. were also partially supported by NSF DBI-2243257. Research reported in this publication by Z.R.T. was supported by the Cancer Center at Illinois–Beckman Institute Postdoctoral Fellows Program, sponsored by the Cancer Center at Illinois and the Beckman Institute for Advanced Science and Technology, University of Illinois Urbana–Champaign. The content is solely the responsibility of the authors and does not necessarily represent the official views of the program sponsors.

References

1. Bianchi DM, Peterson JR, Earnest TM, Hallock MJ, Luthey-Schulten Z. Hybrid CME–ODE method for efficient simulation of the galactose switch in yeast. IET Systems Biology. 2018;12(4):170–176. doi:10.1049/iet-syb.2017.0070.
2. Karr JR, Sanghvi JC, Macklin DN, Gutschow MV, Jacobs JM, Bolival B, et al. A Whole-Cell Computational Model Predicts Phenotype from Genotype. Cell;150(2):389–401. doi:10.1016/j.cell.2012.05.044.
3. Salvy P, Hatzimanikatis V. The ETFL Formulation Allows Multi-Omics Integration in Thermodynamics-Compliant Metabolism and Expression Models. Nature Communications;11(1):30. doi:10.1038/s41467-019-13818-7.
4. Ramsey SA, Smith JJ, Orrell D, Marelli M, Petersen TW, De Atauri P, et al. Dual feedback loops in the GAL regulon suppress cellular heterogeneity in yeast. Nature Genetics. 2006;38(9):1082–1087. doi:10.1038/ng1869.
5. Acar M, Becskei A, Van Oudenaarden A. Enhancement of cellular memory by reducing stochastic transitions. Nature. 2005;435(7039):228–232. doi:10.1038/nature03524.
6. Earnest TM, Watanabe R, Stone JE, Mahamid J, Baumeister W, Villa E, et al. Challenges of Integrating Stochastic Dynamics and Cryo-Electron Tomograms in Whole-Cell Simulations. The Journal of Physical Chemistry B. 2017;121(15):3871–3881. doi:10.1021/acs.jpcb.7b00672.
7. Csárdi G, Franks A, Choi DS, Airoldi EM, Drummond DA. Accounting for Experimental Noise Reveals That mRNA Levels, Amplified by Post-Transcriptional Processes, Largely Determine Steady-State Protein Levels in Yeast. PLOS Genetics. 2015;11(5):e1005206. doi:10.1371/journal.pgen.1005206.
8. Li JJ, Chew GL, Biggin MD. Quantitating translational control: mRNA abundance-dependent and independent contributions and the mRNA sequences that specify them. Nucleic Acids Research. 2017;45(20):11821–11836. doi:10.1093/nar/gkx898.
9. Kremer JR, Mastronarde DN, McIntosh JR. Computer Visualization of Three-Dimensional Image Data Using IMOD. Journal of Structural Biology. 1996;116(1):71–76. doi:10.1006/jsbi.1996.0013.
10. Wei D, Jacobs S, Modla S, Zhang S, Young CL, Cirino R, et al. High-Resolution Three-Dimensional Reconstruction of a Whole Yeast Cell Using Focused-Ion Beam Scanning Electron Microscopy. BioTechniques. 2012;53(1):41–48. doi:10.2144/000113850.
11. Milo R, Jorgensen P, Moran U, Weber G, Springer M. BioNumbers—the database of key numbers in molecular and cell biology. Nucleic Acids Research. 2010;38(suppl_1):D750–D753. doi:10.1093/nar/gkp889.
12. Visser W, Van Spronsen EA, Nanninga N, Pronk JT, Kuenen JG, Van Dijken JP. Effects of growth conditions on mitochondrial morphology inSaccharomyces cerevisiae. Antonie van Leeuwenhoek. 1995;67(3):243–253. doi:10.1007/BF00873688.
13. Verschoor A, Warner JR, Srivastava S, Grassucci RA, Frank J. Three-dimensional structure of the yeast ribosome. Nucleic Acids Research. 1998;26(2):655–661. doi:10.1093/nar/26.2.655.

14. von der Haar T. A quantitative estimation of the global translational activity in logarithmically growing yeast cells. BMC systems biology. 2008;2:87. doi:10.1186/1752-0509-2-87.

15. Yamaguchi M, Namiki Y, Okada H, Mori Y, Furukawa H, Wang J, et al. Structome of Saccharomyces cerevisiae determined by freeze-substitution and serial ultrathin-sectioning electron microscopy. Microscopy. 2011;60(5):321–335. doi:10.1093/jmicro/dfr052.

16. Biswas SK. Quantitative three-dimensional structural analysis of Exophiala dermatitidis yeast cells by freeze-substitution and serial ultrathin sectioning. Journal of Electron Microscopy. 2003;52(>2):133–143. doi:10.1093/jmicro/52.2.133.

17. Warner JR. The economics of ribosome biosynthesis in yeast. Trends in Biochemical Sciences. 1999;24(11):437–440. doi:10.1016/S0968-0004(99)01460-7.

18. Manford AG, Stefan CJ, Yuan HL, MacGurn JA, Emr SD. ER-to-Plasma Membrane Tethering Proteins Regulate Cell Signaling and ER Morphology. Developmental Cell. 2012;23(6):1129–1140. doi:10.1016/j.devcel.2012.11.004.

19. Obara CJ, Moore AS, Lippincott-Schwartz J. Structural Diversity within the Endoplasmic Reticulum—From the Microscale to the Nanoscale. Cold Spring Harbor Perspectives in Biology. 2023;15(6):a041259. doi:10.1101/cshperspect.a041259.

20. Holcman D, Parutto P, Chambers JE, Fantham M, Young LJ, Marciniak SJ, et al. Single particle trajectories reveal active endoplasmic reticulum luminal flow. Nature Cell Biology. 2018;20(10):1118–1125. doi:10.1038/s41556-018-0192-2.

21. Gallo A, Vannier C, Galli T. Endoplasmic Reticulum–Plasma Membrane Associations: Structures and Functions. Annual Review of Cell and Developmental Biology. 2016;32(Volume 32, 2016):279–301. doi:10.1146/annurev-cellbio-111315-125024.

22. West M, Zurek N, Hoenger A, Voeltz GK. A 3D analysis of yeast ER structure reveals how ER domains are organized by membrane curvature. Journal of Cell Biology. 2011;193(2):333–346. doi:10.1083/jcb.201011039.

23. Shibata Y, Voeltz GK, Rapoport TA. Rough Sheets and Smooth Tubules. Cell. 2006;126(3):435–439. doi:10.1016/j.cell.2006.07.019.

24. Xie Y, Shu T, Liu T, Spindler MC, Mahamid J, Hocky GM, et al. Polysome collapse and RNA condensation fluidize the cytoplasm. Molecular Cell. 2024;84(14):2698–2716.

25. de Teresa-Trueba I, Goetz SK, Mattausch A, Stojanovska F, Zimmerli CE, Toro-Nahuelpan M, et al. Convolutional networks for supervised mining of molecular patterns within cellular context. Nature Methods. 2023;20(2):284–294.

26. Lamm L, Zufferey S, Righetto RD, Wietrzynski W, Yamauchi KA, Burt A, et al. MemBrain v2: an end-to-end tool for the analysis of membranes in cryo-electron tomography. biorxiv. 2024; p. 2024–01.

27. Gaifas L, Timmins J, Gutsche I. blik: an extensible napari plugin for cryo-ET data visualisation, annotation and analysis. bioRxiv. 2023; p. 2023–12.

28. Cherry JM, Hong EL, Amundsen C, Balakrishnan R, Binkley G, Chan ET, et al. Saccharomyces Genome Database: the genomics resource of budding yeast. Nucleic Acids Research. 2012;40(D1):D700–D705. doi:10.1093/nar/gkr1029.

29. Roberts E, Stone JE, Luthey-Schulten Z. Lattice microbes: High-performance stochastic simulation method for the reaction-diffusion master equation. Journal of Computational Chemistry. 2013;34(3):245–255. doi:10.1002/jcc.23130.

30. Hallock MJ, Stone JE, Roberts E, Fry C, Luthey-Schulten Z. Simulation of reaction diffusion processes over biologically relevant size and time scales using multi-GPU workstations. Parallel Computing. 2014;40(5):86–99. doi:https://doi.org/10.1016/j.parco.2014.03.009.

31. Gillespie DT. Exact stochastic simulation of coupled chemical reactions. The Journal of Physical Chemistry. 1977;81(25):2340–2361. doi:10.1021/j100540a008.

32. Berg HC, Purcell EM. Physics of chemoreception. Biophysical Journal. 1977;20(2):193–219. doi:10.1016/S0006-3495(77)85544-6.

33. Schuss Z, Singer A, Holcman D. The narrow escape problem for diffusion in cellular microdomains. Proceedings of the National Academy of Sciences of the United States of America. 2007;104(41):16098–16103. doi:10.1073/pnas.0706599104.